Direct 3D Numerical Simulation of Shear Turbulent Mixing

Sin'kova O.G., Statsenko V.P., Yanilkin Yu.V., Zhmaylo V.A.

Paper to be presented at International Workshop on Physics of Compressible Turbulent Mixing (Cambridge, July 2004)

This paper studies shear turbulence growth at a plane interface of two incompressible fluids of constant density using 3D code TREK. The computed data is compared to phenomenological model data and associated well-known experimental data.

Introduction. A simplest shear flow, i.e. one-dimensional unsteady plane mixing layer, is considered. Under certain conditions, many more complex flows are close to it: initial portion of plane and round jets, initial stage of mixing in cylindrical vortex, etc.

Previously [1] we studied the problem using DNS with 2D code [2] and in refs. [3,4] with 3D code [6]. The results were interpreted using a variation of semiempirical theory [7] that includes the Reynolds tensor anisotropy.

This paper studies the problem of shear turbulent mixing at a plane interface of two incompressible fluids of constant density using the DNK with 3D gas-dynamic code TREK [6]. Fluids were considered to be distinctive, i.e. physically immiscible. The computations were performed on a much finer computational grid than in refs. [3, 4].

The turbulent mixing zone width (TMZ), profiles of velocity, turbulent energy, mean-square fluctuations of the longitudinal and transversal velocity components are compared to the measurements of refs. [9-11]. The results of the 3D computations are also compared to the data of the semiempirical theory of turbulence that accounts for the Reynolds tensor anisotropy. The spectral analysis of the velocity fluctuations in the TMZ is conducted. Besides, in contrast to all previous computations for the problem, the concentration probability density function is found from the numerical arrays of the hydrodynamic quantities from 3D computations.

1. Setting up the TREK computations. The problem is formulated much like in refs. [3, 4, 8]: at the initial time two half-spaces separated by a plane interface z= z_c =0 are filled with ideal gases of density ρ_0=1 at pressure p_0=15. In region 1 (concentration c=1) the gas flows parallel to the interface at velocity w≡ $\frac{\partial y}{\partial t}$ = w_0/2 =0.5, in region 2 (concentration c=0) at velocity w = -0.5(Fig.1). The computational domain is a parallelepiped, with its vertical side of the side face being Λ=2. Its horizontal face is a square with side $L_x = L_y$ =1.5.

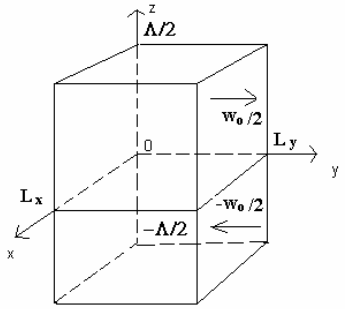

Fig. 1. Geometry of the problem

Here the coordinate of the top face is $z_2 = \Lambda/2$, that of the bottom face is $z_1 = -\Lambda/2$. At the initial time, random perturbations of either of the following two quantities are given at the interface (in a layer one cell thick):

a) density: $\delta\rho = \pm \rho_1 \cdot \delta$, where $\delta = 0.1$.

b) tangent to the boundary of velocity component $w = \pm 0.1\, w_o$.

In so doing we used two sets of random numbers.

The computational grid is uniform (the cell size is $h_x = h_y = h_z$) with $N_x = N_y$, N_z cells. Several computations have been performed, in which L_x/Λ and the number of the cells were varied (see Table 1).

Table 1 – Variants of the computations

Variant No.	Number of cells $N_x x N_y x N_z$	Perturbed quantity	Λ	L_x	Random perturbation spectrum at the boundaries
1	100x100x100	density	1	1	1-st spectrum
2	100x100x100	velocity	1	1	1-st spectrum
3	100x100x100	velocity	1	1	2-nd spectrum
4	150x150x200	velocity	2	1.5	1-st spectrum
5	200x200x400	density	2	1	1-st spectrum
6	300x300x400	density	2	1.5	1-st spectrum

Gas dynamics equations for ideal medium (with zero molecular viscosity) are solved. The equation of state is ideal gas with adiabatic constant $\gamma = 1.4$.

Note that the pressure is such, that in the computations the incompressibility condition was met well for this turbulent flow by virtue of relationship $w_o^2 << \gamma p_o/\rho_o$. The periodicity condition with period L_x was posed on the external region boundaries parallel to OZ and the "rigid wall" condition on the others.

2. Results of 3D computations: integral characteristics. The results of the computations are shown in Figs. 1 through 4 as raster patterns of the velocity components for different times,

in different sections normal to the interface, but parallel to the initial velocity (sections x=const). A feature common to all the variants is the most "smoothed" pattern for the component u_y directed "with stream" (unperturbed). For u_z the pattern is less smoothed, but, like for u_y, regular large vortices are observed. Irregular small-scale perturbations are most characteristic of u_x, see also below. Thus, the largest vortices are of two-dimensional nature and revolve about the axis directed along OX.

The flow evolution as a whole is similar to the previous computations [1, 3-4]: vortex enlargement with time and tapering-off to the self-similar regime are observed.

For this stage the latter manifests itself, in particular, as tapering-off to the linear time dependence of TMZ width $L_t(t)$. Here $L_t \equiv z_2 - z_1$ is the TMZ width in z direction that is determined from points z_1, z_2, at which small enough value ε of an averaged hydrodynamic quantity, for example, concentration $<c_2>(z)$ or velocity $w(z)\equiv<u_y>$, is reached. The averaging was in plane z=const parallel to the interface plane.

Next, assume that $c(z_1)=\varepsilon$, $c(z_2)=1-\varepsilon$, $c \equiv < c_2 >$ is the mass fraction of the material, whose velocity was w_o at the initial time. In another way, $w(z_1)= -(1-\varepsilon)w_o/2$, $w(z_2)=(1-\varepsilon)w_o/2$. Below we assume ε=0.1.

The curve $L_t(t)$ is shown in Fig.5 for all the computation variants. Relevant straight line $L_{appr}(t)$, a linear approximation with $\dot{L}$=const that is closest to the 3D computation results for a given variant, is also plotted for each of the variants. $\dot{L}$ at the self-similar stage is presented in Table 2; it is seen to be about the same in all the variants with accuracy to its estimation error. Maximum scaled turbulent energies k_m at the self-similar stage are also close in the two variants (see Table 2).

Table 2 – Integral values

Variant No.	Number of cells $N_xxN_yxN_z$	Λ	L_x	$\dot{L}$	k_m
1	100^3	1	1	0.1	0.033-0.037
2	100^3	1	1	0.1	0.027
3	100^3	1	1	0.09	0.036
4	150^2x200	2	1.5	0.1	0.037
5	200^2x400	2	1	0.1-0.115	0.042
6	300^2x400	2	1.5	0.08-0.09	0.0342

The results of the computations are also illustrated in Fig.6 plotting $\sigma=1.85\Delta y/\Delta z$. In the latter case, as in ref. [1], length $(y-y_o)$ of the jet appearing in the experiments is related to time $(t-t_o)$:

$$(y-y_o)=(w_1+w_2)(t-t_o)=\frac{(1+m)w_o(t-t_o)}{2(1-m)};$$

$$m\equiv\frac{w_2}{w_1};\qquad w_o\equiv w_1-w_2.$$

Each $\dot{L}\equiv\frac{dL_t}{dt}$ is therewith correspondent with a curve in Fig. 6.

In Fig. 6 different points show experimental data of different authors that are presented in refs. [9, 10]. As seen, there is a satisfactory agreement with the experiments for all the variants.

The self-similar regime of this problem is also correspondent with the tapering-off to the stationary value $k_m(t)\equiv\max(k)$ – the TMZ width maximum turbulent energy is $k(z)=E_{ii}$, where $E_{ik}(z)\equiv\frac{<u_iu_k>-<u_i><u_k>}{2}$, the averaging (denoted with < >) is performed over the entire section z=const.

The curve $k_m(t)$ is plotted in Fig. 7. As seen from the figure (see also Table 2), in all the 3D computations the maximum values of k_m are quite close.

In the self-similar regime, the value of the velocity fluctuation anisotropy (Reynolds number) characteristic of TMZ must be stationary:

$$A_{ik}(t)\equiv\max(E_{ii})/\max(E_{kk}) \qquad , \tag{1}$$

where TMZ width maximum diagonal components of tensor (1) appear – there are no summation over subscripts i, k.

The results in the form of time dependence of A_{ik} are shown in Fig. 8. As seen, the Reynolds tensor anisotropy is pronounced in the 3D computations, with the "longitudinal" component of the turbulent energy (i.e. of the diagonal part of Reynolds tensor E_{ii}) being larger than the "transversal" components in the mixing zone.

According to turbulence model [7] including the Reynolds tensor anisotropy, relations

$$R_{xx}=R_{zz};\qquad A_{zy}=\frac{R_{zz}}{R_{yy}}=\frac{1/3-b}{1/3+2b} \tag{2}$$

are valid.

For most variants the results agree with (2) at the self-similar stage.

3. Profiles of the quantities in the 3D computation. Fig. 9 plots the velocity profiles for the self-similar stage of the variants under discussion. The argument is

$$\eta \equiv \frac{z - z_c}{w_0 (t - t_0)},$$

here t_0 for each variant is found from Fig. (9) reasoning from condition $L_{appr}(t_0) = 0$.

As seen from Fig. 9, the agreement between the computed velocity profiles and the ones measured in refs. [8,9] is satisfactory.

Turbulent energy profiles $k(\eta)$ for the self-similar stage of the variants under consideration are shown in Fig. 10. As seen, the computations lead to a satisfactory agreement with the measurements of refs. [8,9] (in the experimental data processing we assumed that the two transversal velocity fluctuation components were equal). The same is true for the mean-square fluctuation profiles of longitudinal velocity component $u'_y \equiv \sqrt{E_{yy}}$ shown in Fig. 11 as well as for those of transversal velocity component $u'_z \equiv \sqrt{E_{zz}}$ that are shown in Fig. 12: the agreement between the computations and the measurements of ref. [9] is satisfactory on the whole.

4. Velocity fluctuation spectra. The computed data was used as a basis to study the velocity fluctuation spectrum in accordance with formula

$$\begin{aligned} &E_{il}^{(n)}(x,y) = \langle u_i^2 \rangle_{|_{l,x,y,z}} - \langle u_i \rangle^2_{|_{l,x,y,z}}; \qquad n = 1,2....N_z \\ &E_{il}(z) = E_{il}^{(n)} = \langle E_{il}^{(n)}(x,y) \rangle; \qquad l = rh, \qquad r = 2,3....N_x. \end{aligned} \quad . \tag{3}$$

Here the averaging $\langle\rangle_{|_{l,x,y,z}}$ is performed in the n-th layer (over z) in a square with side l (l=rh, h is the computational cell size), whose center coordinates are x, y, z, and then the averaging ($\langle\rangle$) is over all possible values of x, y in the squares with the value of l in the entire n-th layer. There is no summation over **i** in (4). Next:

$$\mathrm{E_l} = \sum_{\mathrm{i=1}}^{\mathrm{i=3}} \mathrm{E_{iil}} \ .$$

The computed data for several times in different variants are presented in Figs. 13 and 14 as curves $\lg E_{il}(\lg K)$, $\lg E_l(\lg K)$ (where K=2π/l) for different values of the scaled coordinate $\zeta \equiv \frac{z - z_c}{L_t}$. The figures also give Kolmogorov spectrum

$$\mathrm{lgE_l = -2/3\ lgK + const.}$$

As seen, inside the TMZ (0.4> ζ > -0.4) there are intervals of wave numbers K, on which the spectrum of total energy $\mathrm{E_l}$ is close on the whole to the 3D Kolmogorov spectrum. Also note that on small space scales (high K) the velocity fluctuations become anisotropic: the x

component becomes dominant, whereas the z component and particularly the y component are inhibited dramatically.

This is just in what the problem under discussion differs from the gravitational turbulent mixing, in whose modeling (see [11]) the velocity fluctuations, conversely, become isotropic at high K – all components E_{iil} become close. A reason for this is that for the gravitational turbulent mixing the averaged velocity is zero, whereas for the shear mixing it is nonzero. In this case the role of the scheme viscosity manifests itself significantly. The numerical technique TREK employs the difference scheme of the first approximation order, whose scheme viscosity can be evaluated in the event of quasi-stationary flows by writing the momentum transfer equations as follows:

$$\begin{aligned}
&\frac{\partial \rho u_x}{\partial t} + div\,\rho u_x \vec{u} + \frac{\partial P}{\partial x} = \frac{\partial}{\partial x}\left(\frac{h}{4}\rho u_x \frac{\partial u_x}{\partial x}\right) + \frac{\partial}{\partial y}\left(\frac{h}{4}\rho u_y \frac{\partial u_x}{\partial y}\right) + \frac{\partial}{\partial z}\left(\frac{h}{4}\rho u_z \frac{\partial u_x}{\partial z}\right) + \theta_1\left(h^2, \tau^2\right), \\
&\frac{\partial \rho u_y}{\partial t} + div\,\rho u_y \vec{u} + \frac{\partial P}{\partial y} = \frac{\partial}{\partial x}\left(\frac{h}{4}\rho u_x \frac{\partial u_y}{\partial x}\right) + \frac{\partial}{\partial y}\left(\frac{h}{4}\rho u_y \frac{\partial u_y}{\partial y}\right) + \frac{\partial}{\partial z}\left(\frac{h}{4}\rho u_z \frac{\partial u_y}{\partial z}\right) + \theta_2\left(h^2, \tau^2\right), \\
&\frac{\partial \rho u_z}{\partial t} + div\,\rho u_z \vec{u} + \frac{\partial P}{\partial z} = \frac{\partial}{\partial x}\left(\frac{h}{4}\rho u_x \frac{\partial u_z}{\partial x}\right) + \frac{\partial}{\partial y}\left(\frac{h}{4}\rho u_y \frac{\partial u_z}{\partial y}\right) + \frac{\partial}{\partial z}\left(\frac{h}{4}\rho u_z \frac{\partial u_z}{\partial z}\right) + \theta_2\left(h^2, \tau^2\right).
\end{aligned} \tag{4}$$

The right-hand sides of equations (4) can be treated as derivatives of the approximation viscosity stress "tensor" components. They can be written as:

$$\sigma_{ik} = \frac{1}{4} h \rho u_k \frac{\partial u_i}{\partial x_k}\ , \tag{5}$$

where u_k is the characteristic flow velocity. We put the term "tensor" in quotes, as neither (4) nor (5) is a tensor.

Nevertheless, relation (5) is similar in its form to the expression for the viscous stress tensor components appearing in the Navier-Stokes equations. Here the role of the molecular viscosity factor, which is a scalar, is played by the scheme viscosity factor, which is a vector

$$\mu_{ck} = \frac{1}{4} h \rho u_k\,, \quad \nu_{ck} = \frac{1}{4} h u_k$$

depending on the flow velocity and computational cell size h.

Evidently, the scheme viscosity effect should show up most of all at the smallest scales (high K), which is just observed in Figs. 13 and 14. As mentioned in Section 2, the largest shear flow vortices are of 2D nature and rotate about the axis directed along OX. Then not only the largest average component u_y, but also quite large component u_z will influence the scheme effects on small scales. It is these components, in contrast to u_x (the average of which are zero on nearly all scales), that should be inhibited to the largest extent on these scales, which is just confirmed by Figs. 13 and 14. On a finer grid the scheme viscosity effect should be smaller and

the spectrum closer to the Kolmogorov spectrum. This is confirmed by the comparison between Fig. 13 and Fig. 14 for variant 5 on a finer grid.

On large scales (low K), either y or (in some points) x velocity fluctuation component is predominant.

5. Concentration probability density function

The data from the numerical computation has been used to determine the one-point mass concentration probability distribution density function for the material that initially had velocity $w \equiv \frac{\partial}{\partial} \frac{y}{t} = w_o/2 = 0.5$ and coordinate $z > z_c$

$$F(c,z,t) = \frac{N(c^{(ik)}(z) \geq c) - N(c^{(ik)}(z) \geq (c + \Delta c))}{N_0 \Delta c},$$

here $N(c^{(ik)}(z) \geq c)$ is the number of points in a given horizontal plane z, at which the current concentration $c^{(ik)}$ is larger than c; $N_o(z)$ is the total number of points in the plane. The c runs a range of M numbers $c = (0, 1, 2, ..., M-1)\Delta c$, where: $M\Delta c = 1$; in our computations, M=100.

Recall that before determination of F(**c**) the concentration array is averaged according to formula

$$c^{(n)}(l,x,y,z) = \langle c \rangle_{|_{l,x,y,z}}; \qquad n = 1,2....N_z$$

where l=rh, r=2. In fact, for r≥2 (but $r << \min(N_x, N_y)$) the resultant functions F(**c**) differ insignificantly, whereas for r=1 the difference is drastic: the F(**c**) is close to two δ functions, δ(0) and δ(1).

As Figs. 15 and 16 show, the form of the function F(**c**) in variant 6 is much alike for times t=6.2 and t=9. Near the TMZ boundary adjacent to the material of initial concentration **c**=1 ($\zeta \equiv \frac{z - z_c}{L_t} = 0.49$), the maximum values of F(**c**) are mainly near **c**≈1. The F(**c**) is therewith concentrated in a narrow region **c**≈1 (it has the form of the δ function), while in the major range of **c** it is essentially constant and small (F(**c**)<0.2).

Inside the TMZ, as the plane of symmetry ($\zeta = 0$) is approached, the F(**c**) becomes uniformly distributed over the concentration range and increases.

Conclusion. The direct 3D numerical simulation of shear mixing that had been performed with the code TREK [6] showed that the self-similar regime took place on some time interval in all the computations. It is correspondent with constant TMZ width growth rate $\dot{L}$, which is about the same for all the computations. Its value agrees satisfactorily with the experimental data.

TMZ maximum turbulent energies E_m also remain constant in this regime. Its values are also close in all the computations.

For this problem, the self-similar regime also involves the tapering-off to stationary velocity fluctuation anisotropy, in the 3D computation its value is described satisfactorily by the phenomenological model [7] with semiempirical coefficient b=0.085.

For all the variants at the self-similar stage of the computations under discussion, the computed velocity profiles agree satisfactorily with those measured in ref. [9]. The self-similar stage turbulent energy profiles $k(\eta)$ agree satisfactorily with measurements [8,9]. The calculations on a finer computational grid ensure a better agreement with the measurements. The longitudinal and transversal velocity component mean-square fluctuation profiles agree satisfactorily with measurements [9], the best agreement is for the finest computational grid.

Inside TMZ, the spectrum of total energy E_l of velocity fluctuations in the 3D computations is close on the whole to the 3D Kolmogorov spectrum: the finer is the grid, the closer is the spectrum.

There are the following features in the problem, in which it differs from the gravitational mixing problem:

- the largest vortices are of 2D nature and rotate about the axis directed along OX,
- on small scales the x component of velocity fluctuations is dominant, as the scheme viscosity effects inhibit the y component and z component.

As mentioned in Introduction, these computations are close in their setting to the previous computations [3,4], but differ in a significantly finer computational grid. As seen from this paper, the grid provided a significantly better agreement with the experimental data.

This problem clearly demonstrates the possibilities of the 3D shear mixing simulations and, at the same time, reveals demerits of the computational technique used that possesses a dramatic scheme viscosity. It is being planned that the studies would be continued with using other numerical techniques as well.

References

1.Bakhrakh S.M., Zhmailo V.A., Statsenko V.P., Yanilkin Yu.V. Numerical simulations of turbulent mixing in shear flows\\ Chislennye Metody Mekhaniki Sploshnoy Sredy, V. 14, No. 2, P.11-27, Novosibirsk, 1983.

2. Bakhrakh S.M., Glagoleva Yu.P., Samigulin M.S., Frolov V.D., Yanenko N.N. Yanilkin Yu.V. Computation of gas-dynamic flows using the method of concentrations// Doklady AN SSSR, 1981, V.257, No. 3, P.566-569.

3. Zhmailo V.A., Stadnik A.L., Statsenko V.P., Yanilkin Yu.V. Direct numerical simulation of turbulent mixing in shear flows// Voprosy Atomnoy Nauki i Tekhniki, Ser. Teoreticheskaya i Prikladnaya Fizika, 1996, P.43-51.

4. Stadnik A.A., Statsenko V.P., Yanilkin Yu.V., Zhmailo V.A. Direct numerical simulation of turbulent mixing in shear flows // Laser and Particle Beams, Vol.15, N 1, (1997-2). P.115-125.

5. Shanin A.A., Yanilkin Yu.V. Program complex EGAK. Gas-dynamic difference schemes in Eulerian variables// Voprosy Atomnoy Nauki i Tekhniki, Ser. Matematicheskoye Modelirovaniye Fizicheskikh Protsessov, 1993, No.1, P. 24-30.

6. Stadnik A.L., Shanin A.A., Yanilkin Yu.V. Eulerian technique TREK for computations of 3D gas-dynamic multi-material flows// Voprosy Atomnoy Nauki i Tekhniki, Ser. Matematicheskoye Modelirovaniye Fizicheskikh Protsessov, 1994, No.4.

7. Statsenko V.P. Testing the turbulence model with Reynolds tensor anisotropy// Voprosy Atomnoy Nauki i Tekhniki, Ser. Teoreticheskaya i Prikladnaya Fizika, 1996, P.43-51.

8.Spenser B.W., Jones B.G. Statistical investigation of pressure and velocity fields in the turbulent two-stream mixing layers . -AIAA Paper, 1971, P.613.

9.Browand F.K., Latigo B.O. Growth of the two-dimensional mixing layer // Phys.Fluids. 1979. Vol. 22, N 6, P.1011.

10. Rodi W.A. Rewiew of experimental data of uniform density free turbulent boundary layers. -Studies in convection, Acad. Press, London, 1975, Vol 1, P.79-166.

11. Yanilkin Yu.V., Statsenko V.P., Rebrov S.V., Sin'kova O.G., Stadnik A.L. Study of gravitational turbulent mixing at large density differences using direct 3D numerical simulation // Report to 8th International Seminar on Turbulent Mixing of Compressible Matter, Pasadena, USA, 2001.

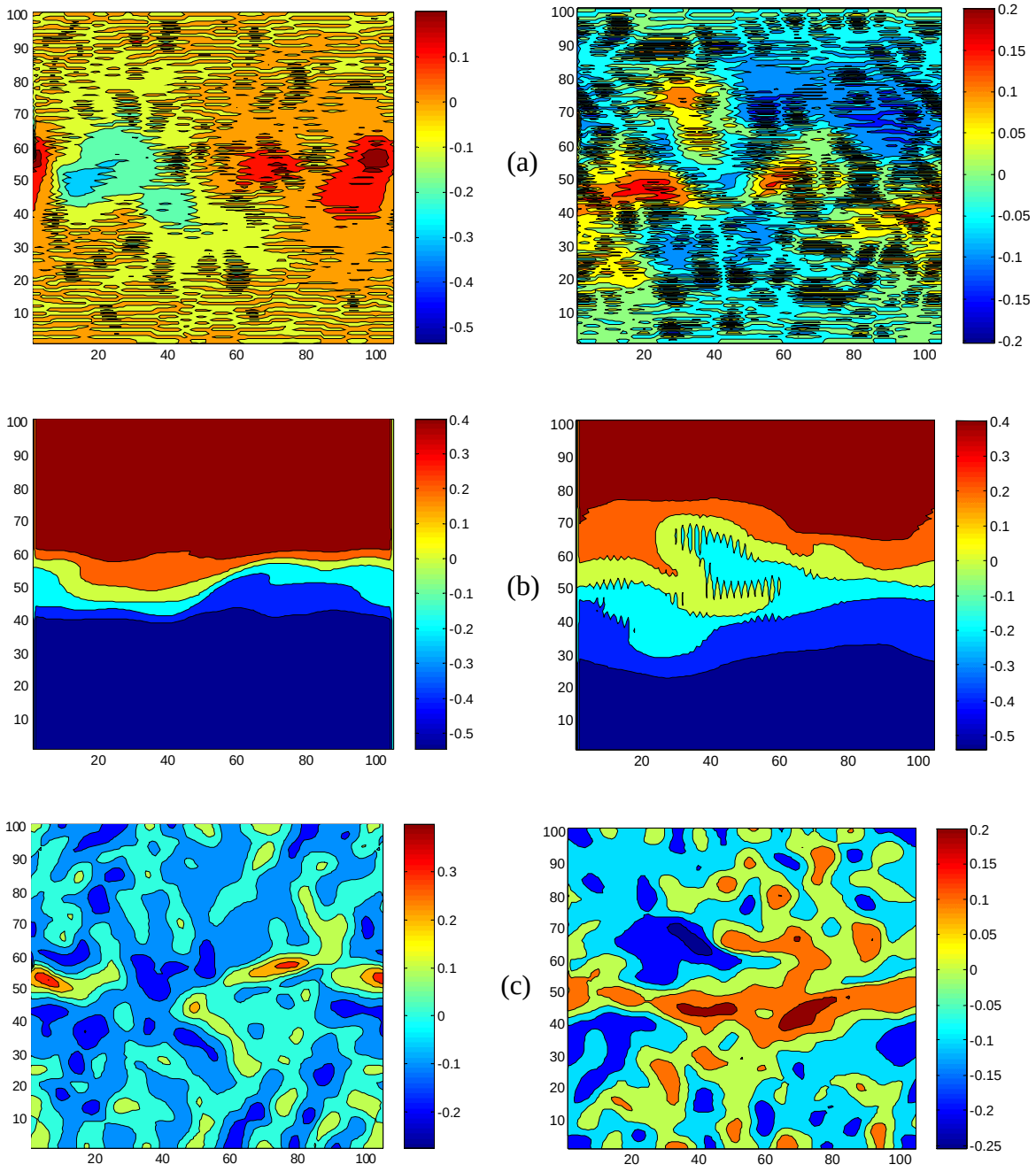

Fig. 1. Raster patterns of velocity components: a) u_z, b) u_y c) u_x; variant 1, x=const (i=50), left: t=4; right: t=8

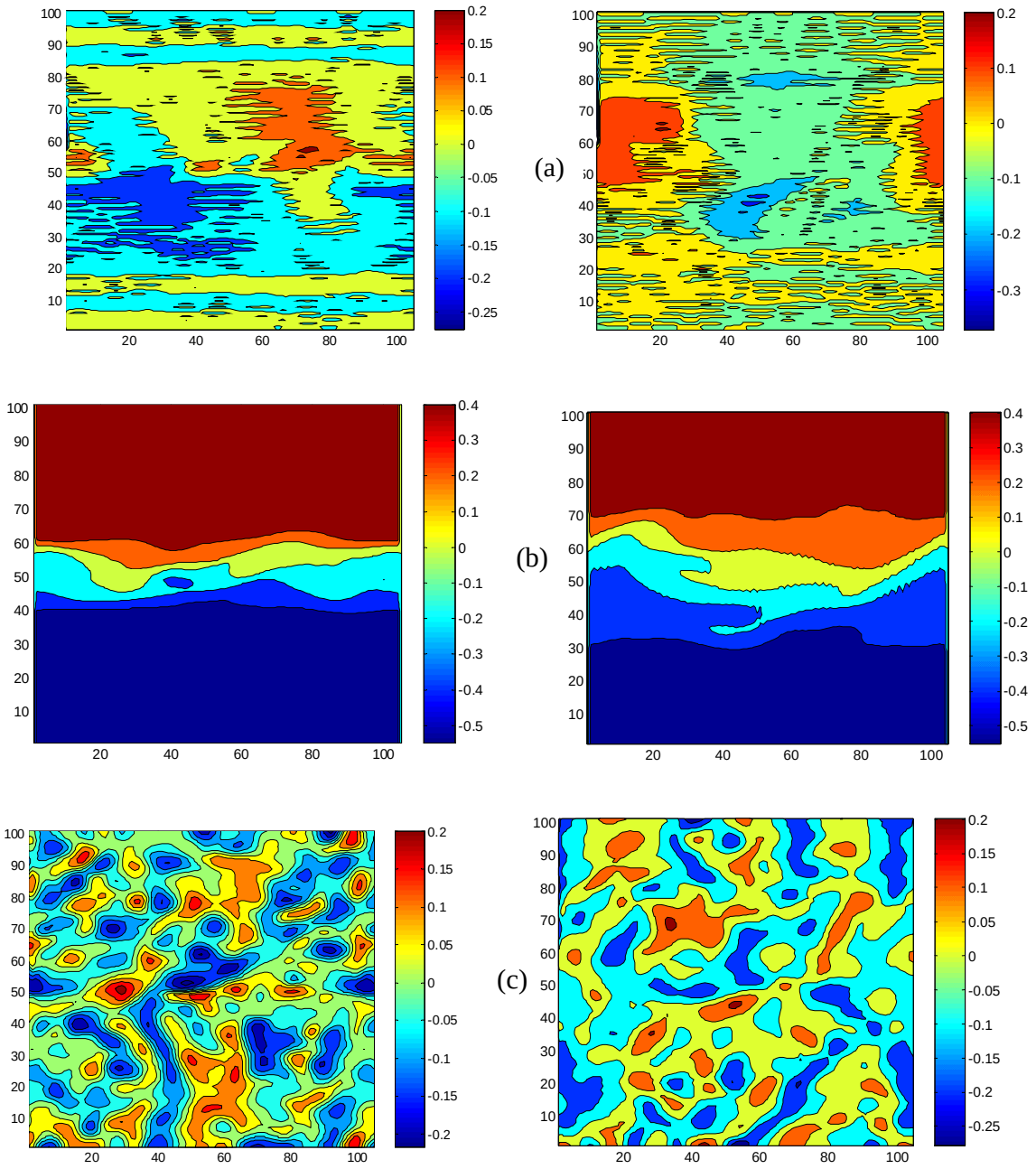

Fig. 2. Raster patterns of velocity components: a) u_z, b) u_y c) u_x; variant 2, x=const (i=50), left: t=3.5; right: t=7.5

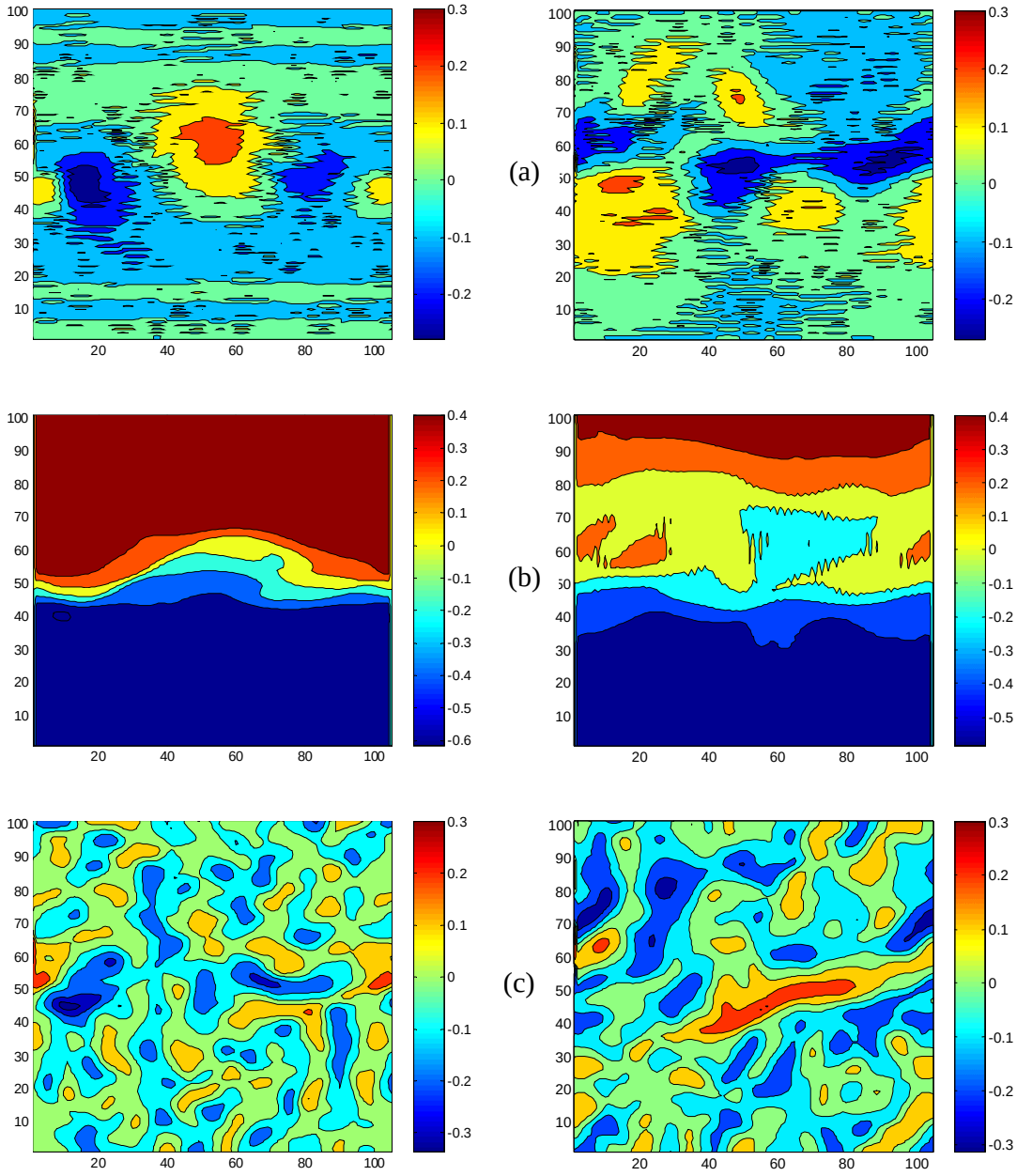

(a)

Fig. 3. Raster patterns of velocity components: a) u_z , b) u_y c) u_x; variant 3, x=const (i=50), left: t=3.5; right: t=8

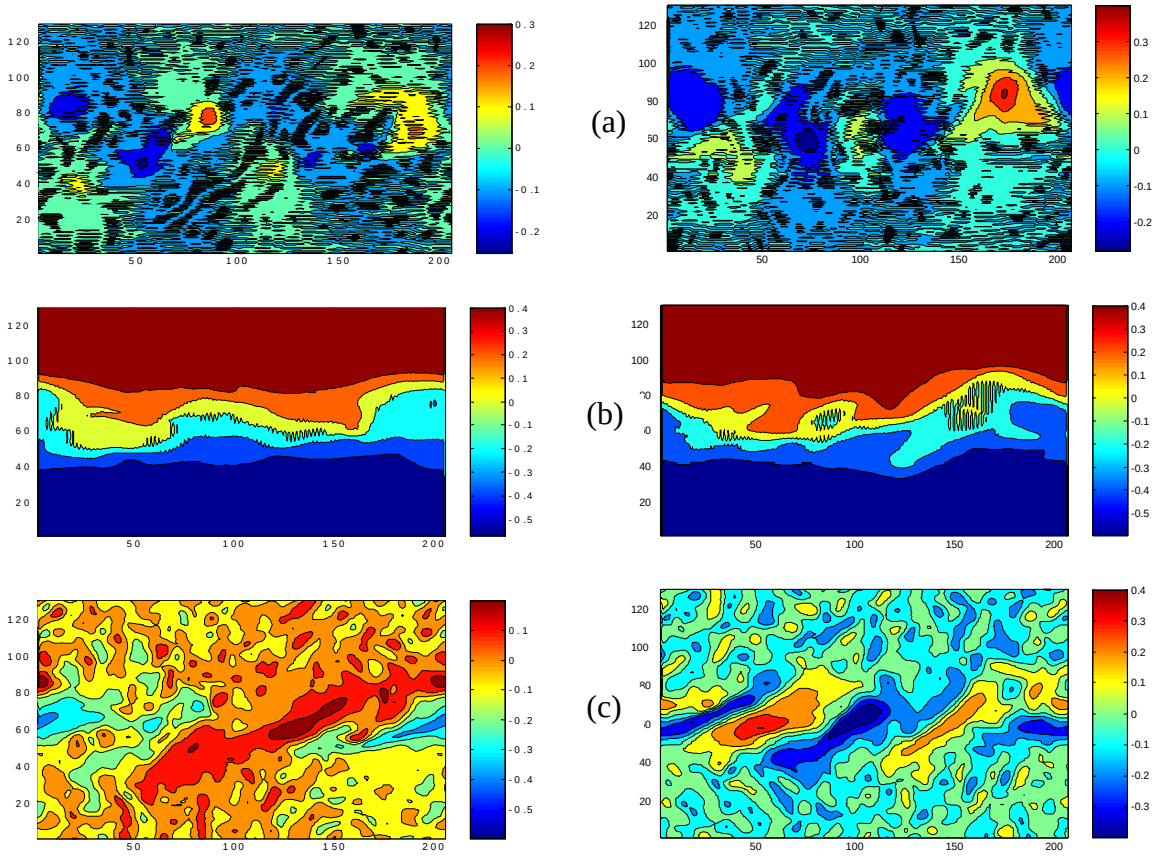

Fig. 4. Raster patterns of velocity components: a) u_z, b) u_y c) u_x; variant 5, слева- x=const (i=150), t=3.5; right: (i=100), t=3.5

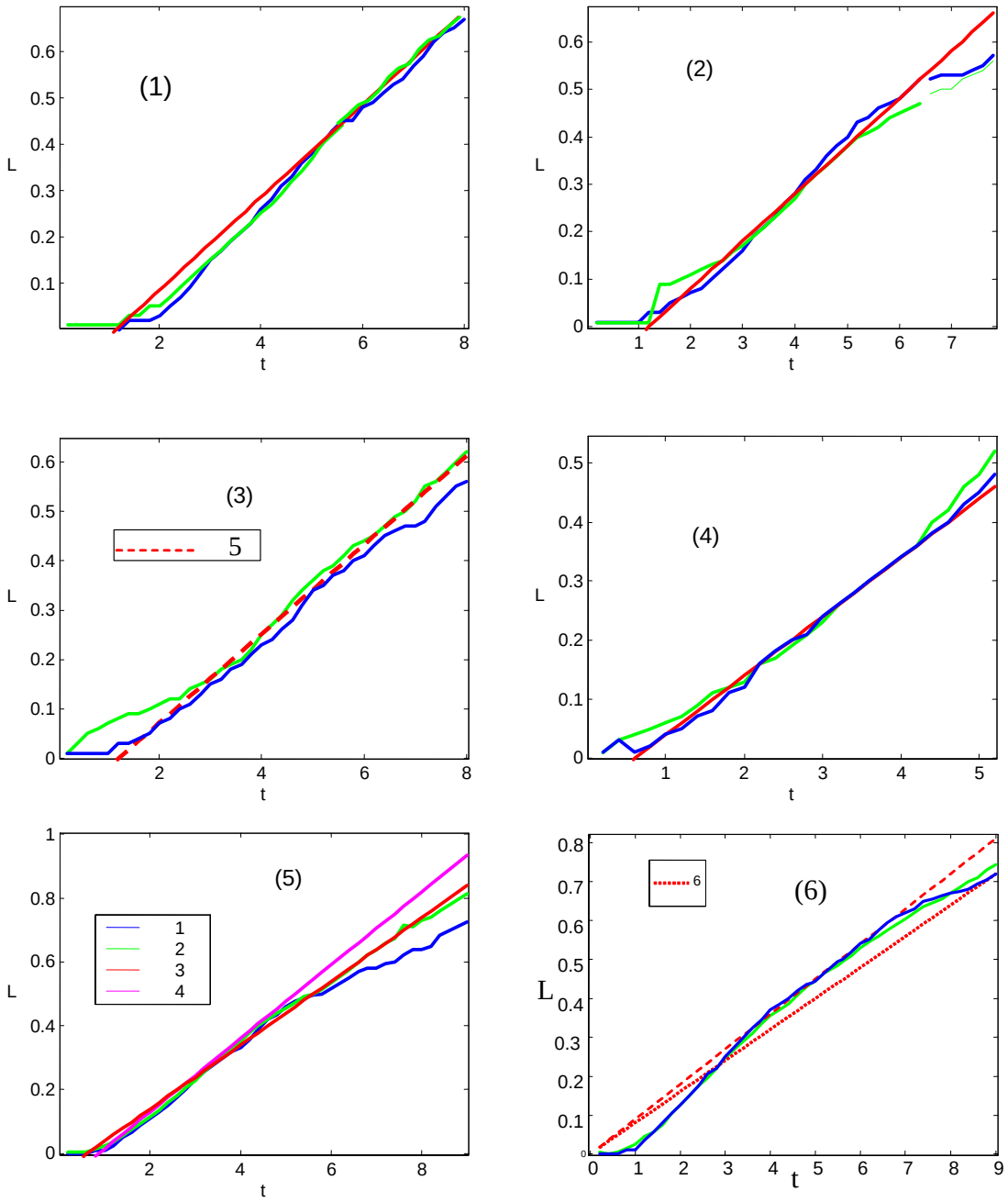

Fig. 5. Turbulent mixing zone width versus time. The variant numbers are specified in the figures. Curve numbers: 1 – L from the concentration profile, 2 – L from the velocity profile; linear approximation: 3 – $\dot{L}$ =0.1, 4 – $\dot{L}$ =0.115, 5 – $\dot{L}$ =0.09, 6 – $\dot{L}$ =0.08

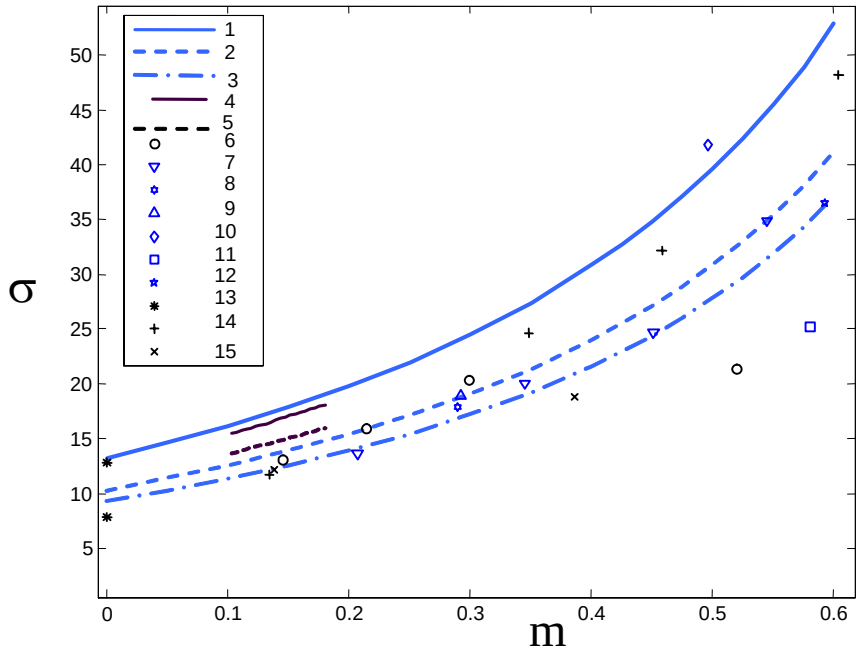

Fig. 6 - Function of mixing rate . 3D computations: 1 - $\dot{L}$ =0.08, 2 - $\dot{L}$ =0.09, 3 - $\dot{L}$ =0.1, 4-5 – experimental data [9], 6-15 –experimental data [10]

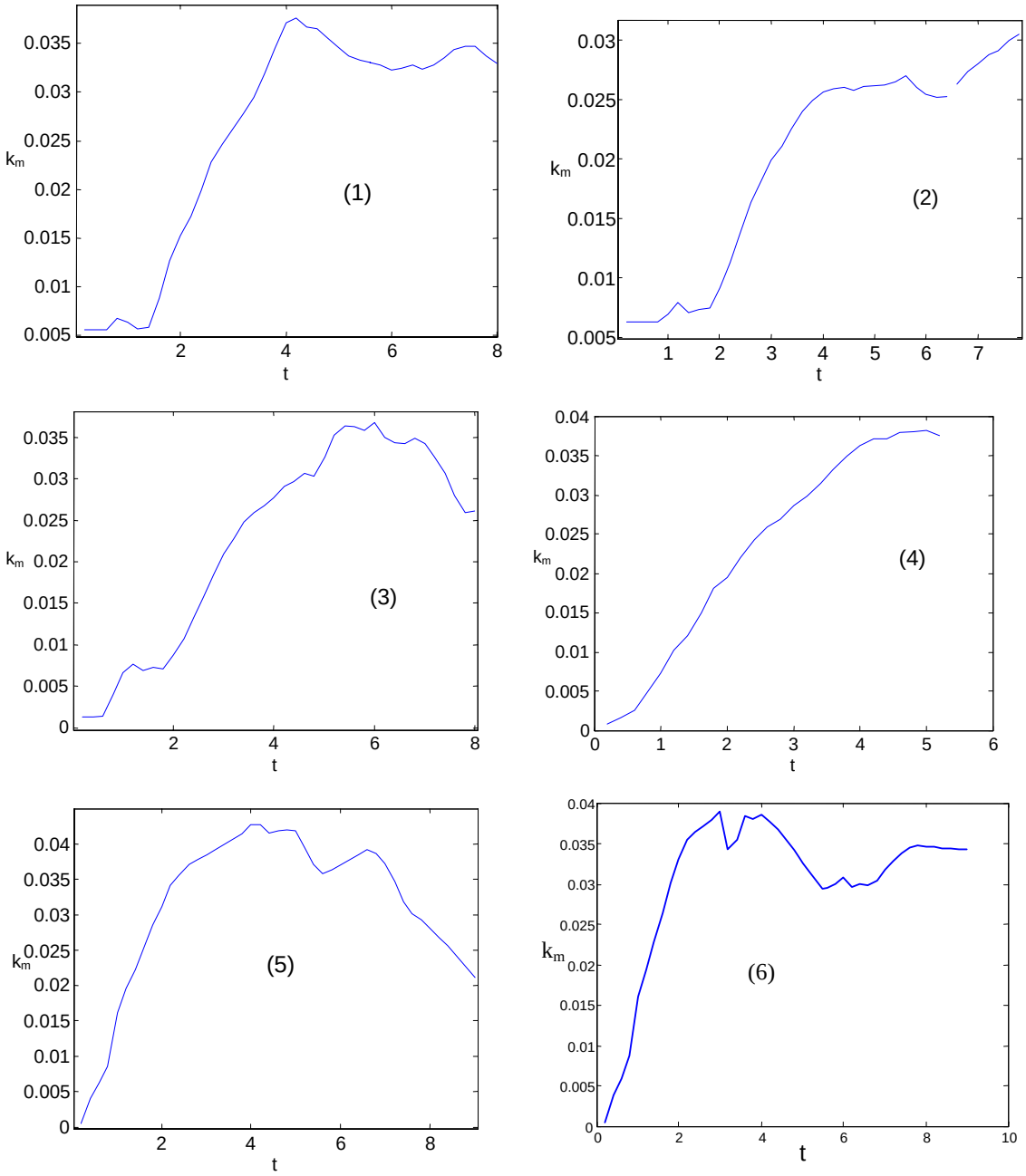

Fig. 7. Zone width maximum turbulent energy versus time. The variant numbers are specified in the figures

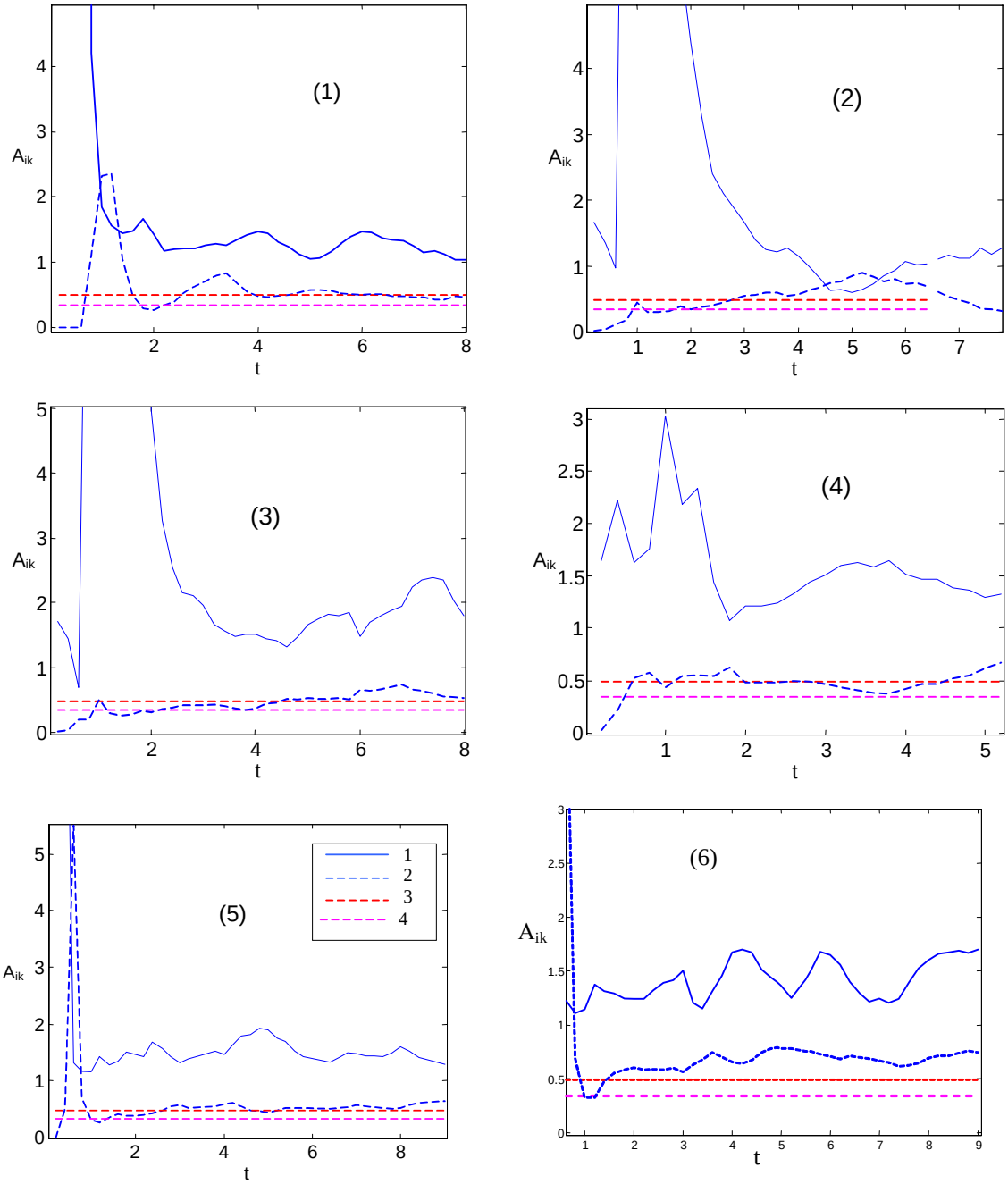

Fig. 8 – Reynolds tensor anisotropy versus time. The variant numbers are specified in the figures. 1 - A_{xz} , 2 - A_{zy} ; A_{zy} from model [7]: 3 – b=0.085, 4 – b=0.13

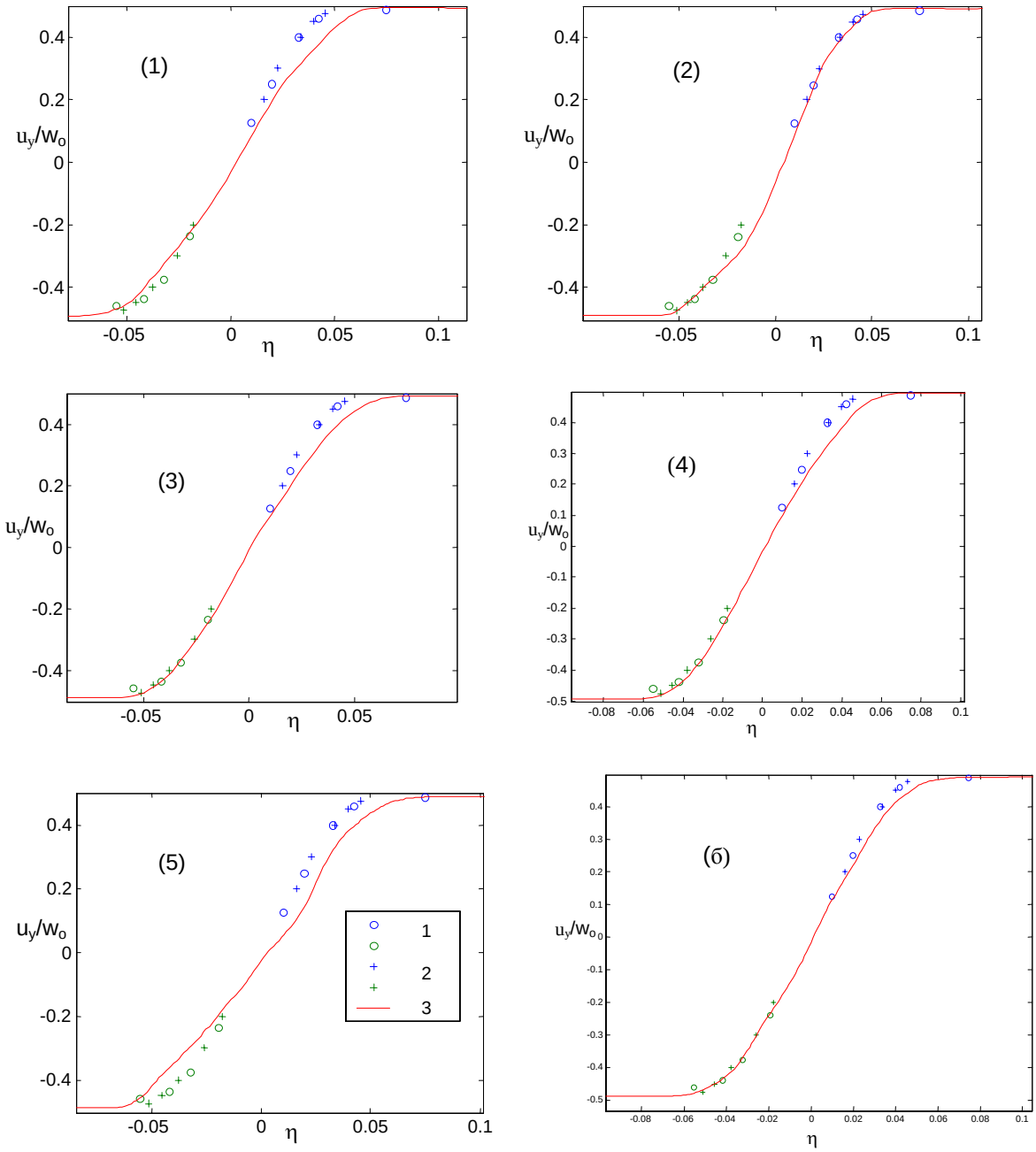

Fig. 9. Velocity profiles. The variant numbers are specified in the figures. 1, 2 – measurements [8,9].

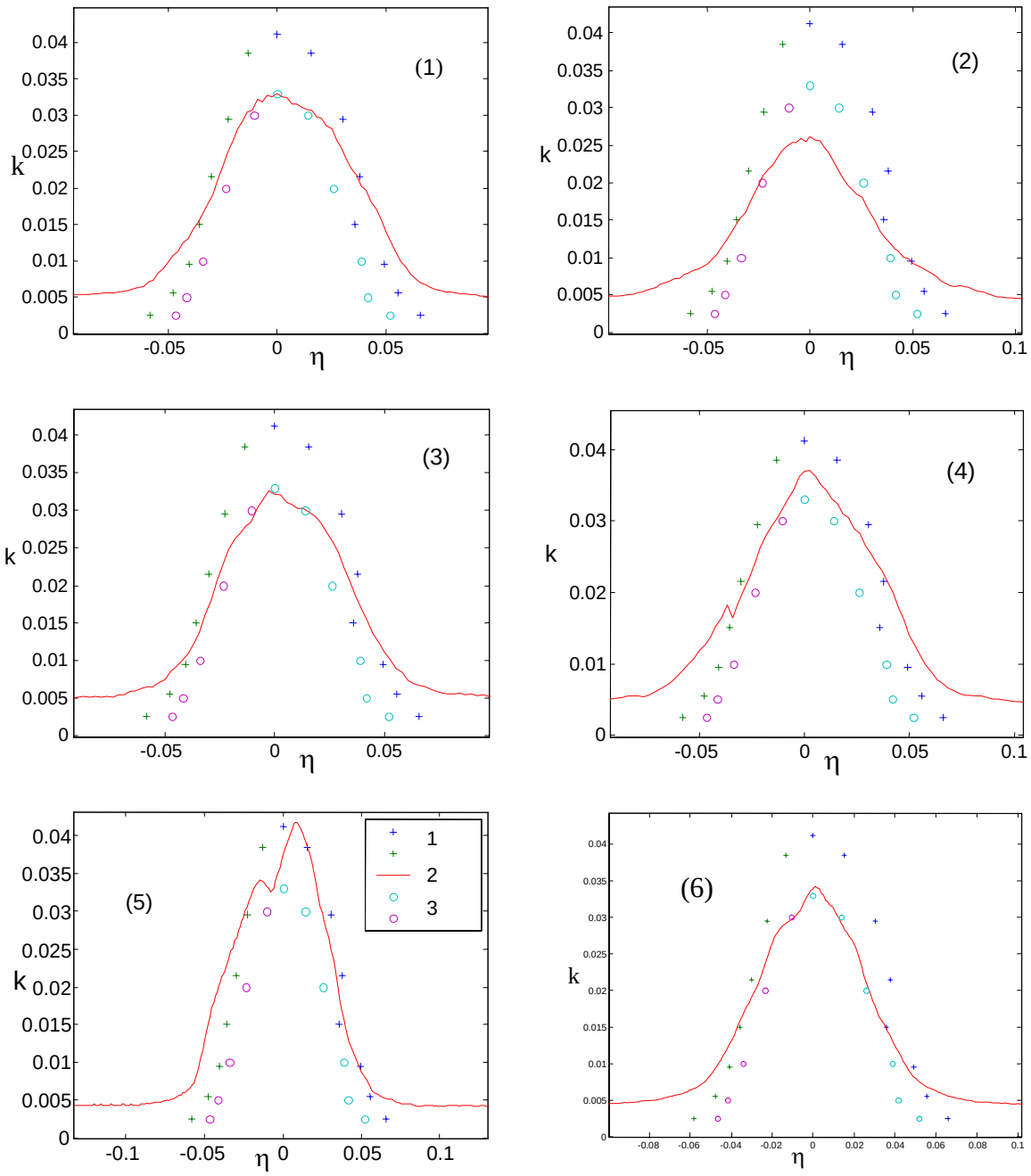

Fig. 10. Turbulent energy profiles. The variant numbers are specified in the figures. 1, 3 – measurements [8,9]

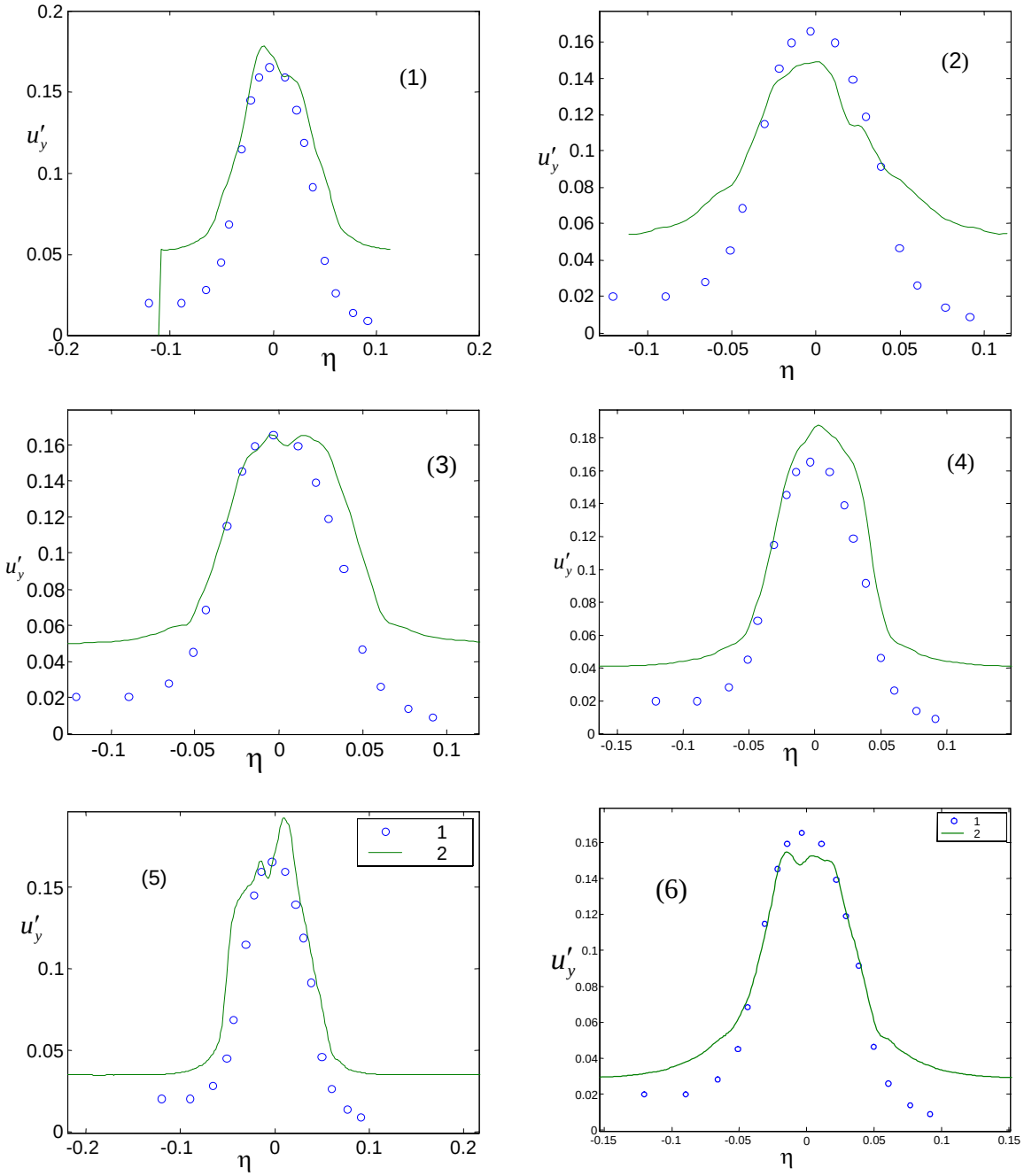

Fig. 11. Longitudinal velocity component mean-square fluctuation profiles. The variant numbers are specified in the figures, 1 – measurements [9], 2 - calculation

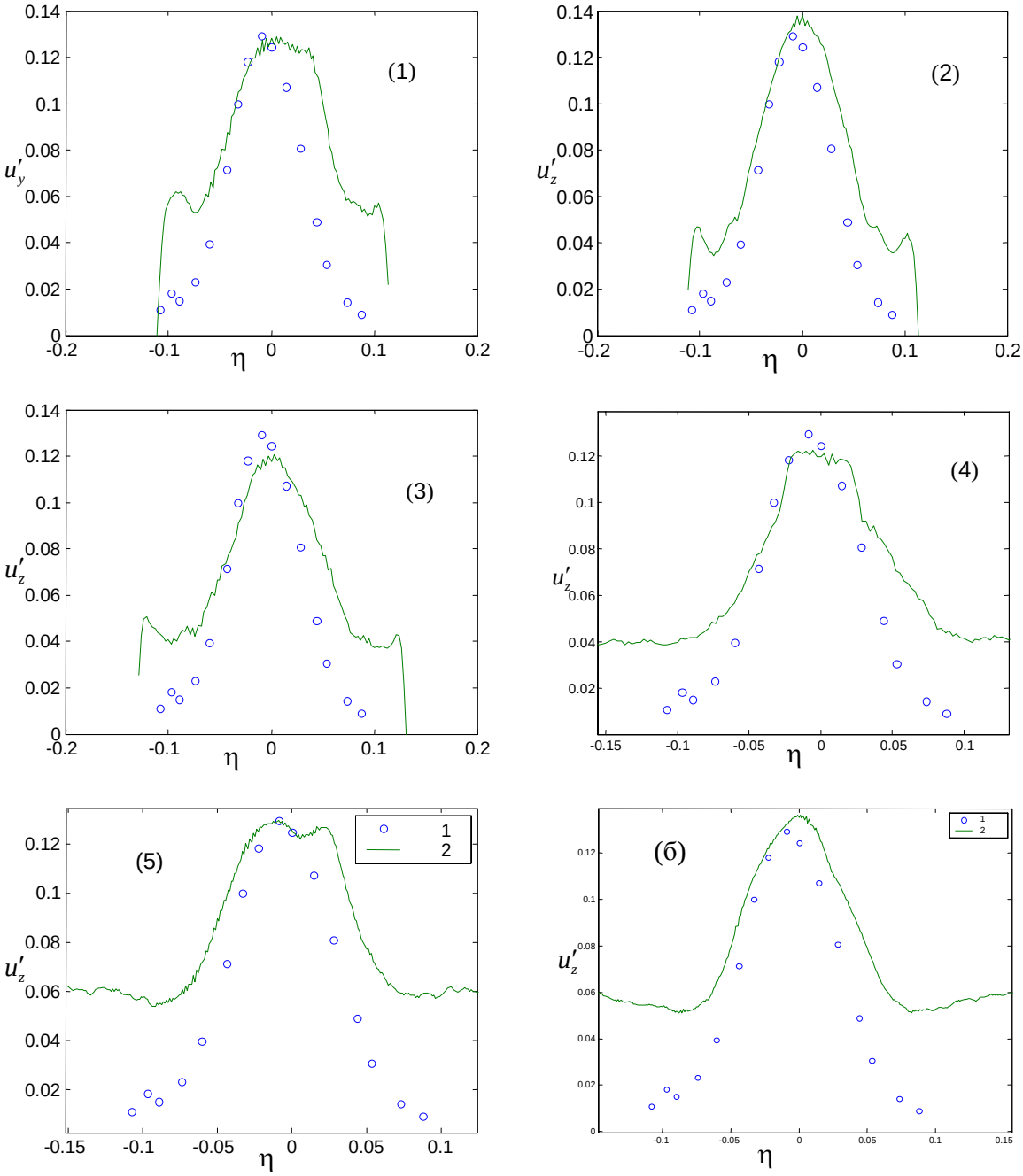

Fig. 12. Transversal velocity component mean-square fluctuation profiles. The variant numbers are specified in the figures . 1 – measurements [9], 2 - calculation

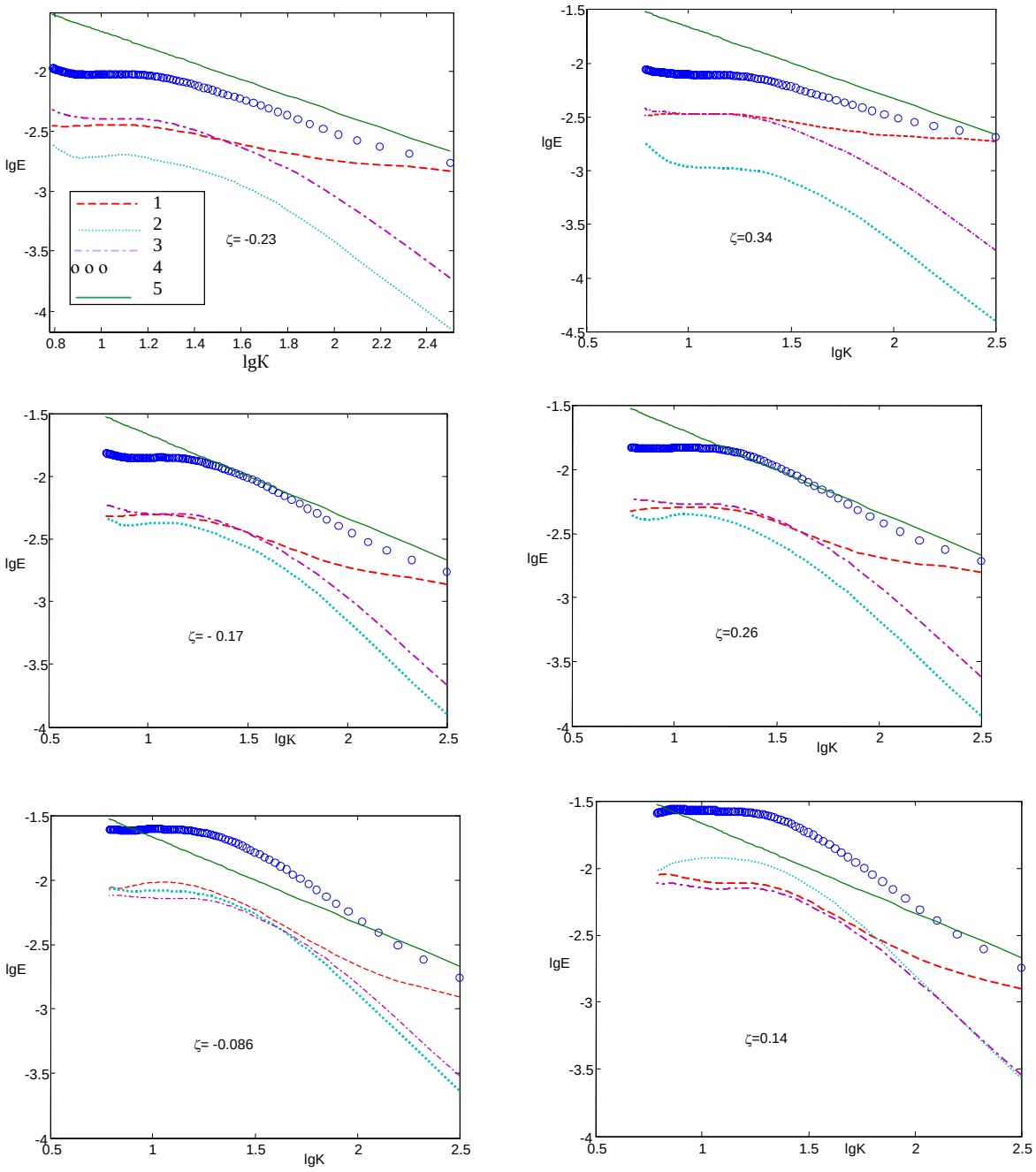

Fig. 13. Velocity fluctuation spectrum, variant 1, t=3.5; 1 - E_{xl}, 2 - E_{yl}, 3 - E_{zl}, 4 – E_{l},; 5 - Kolmogorov spectrum

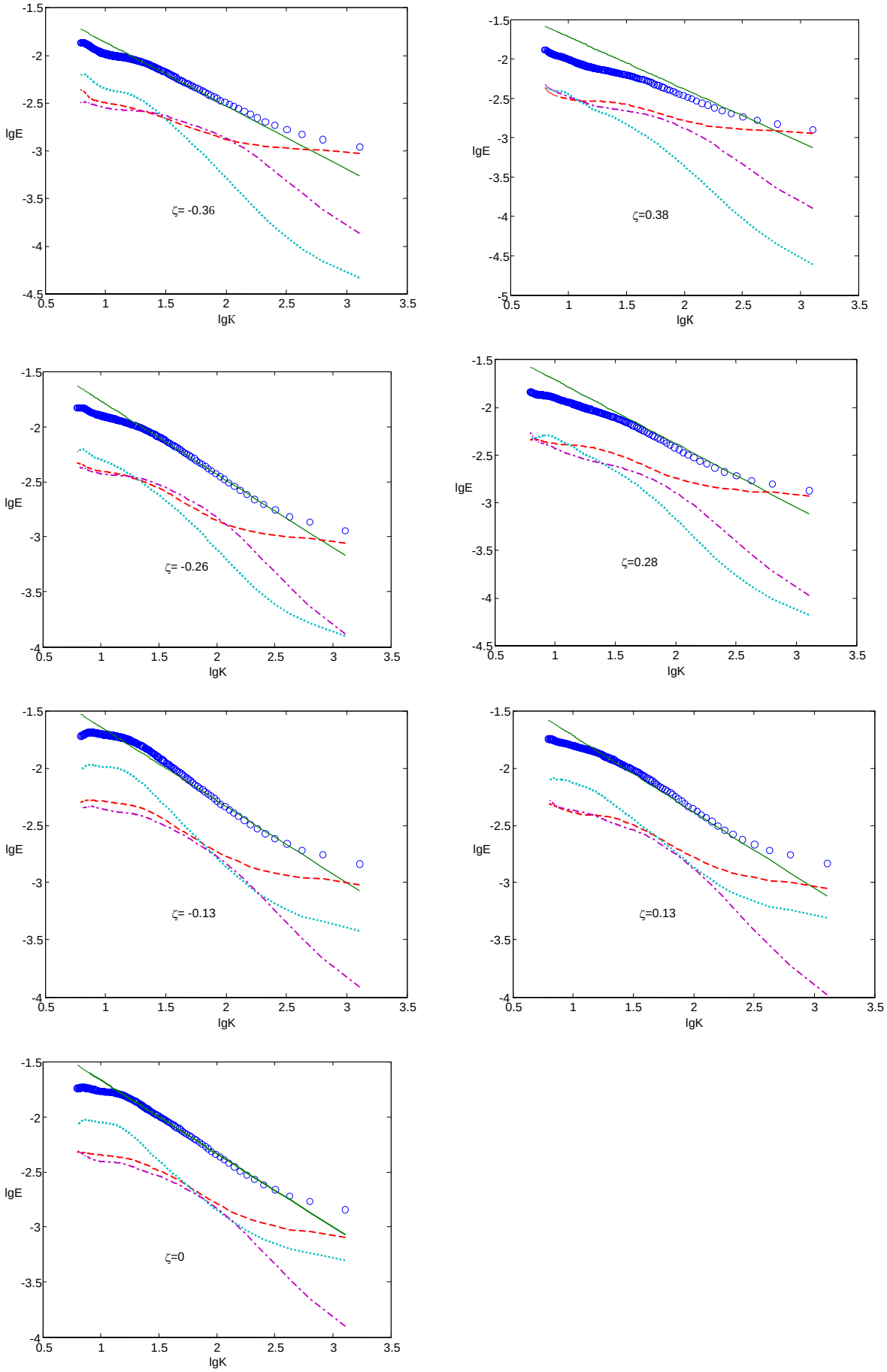

Fig. 14. Velocity fluctuation spectrum, variant 5, t=3.5; the notation is the same as in Fig. 13.

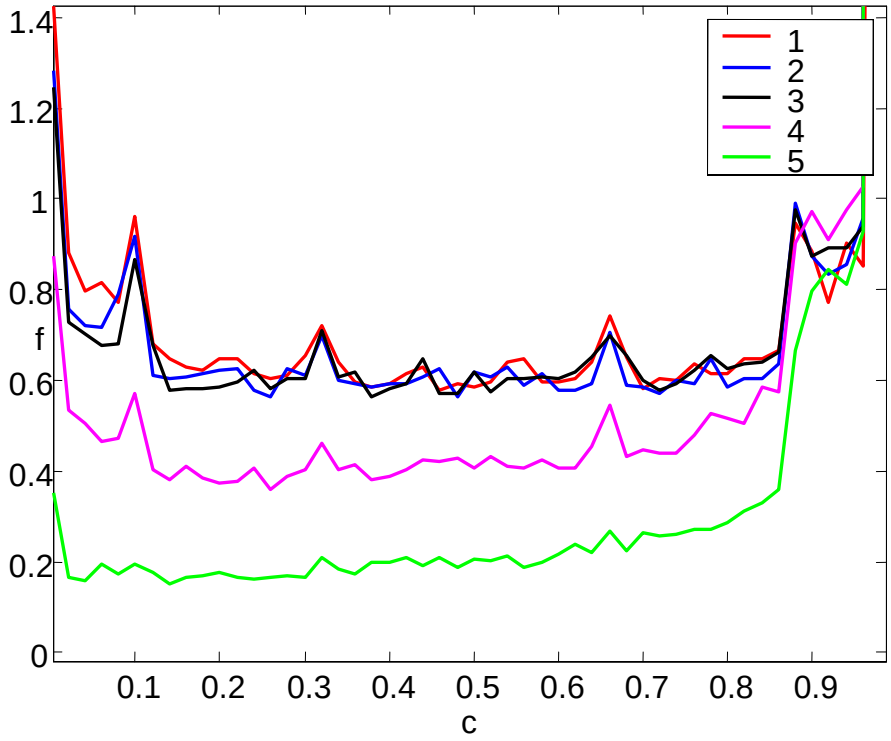

Fig. 15. Probability density function versus concentration in variant 6, t=9 (M=100). Curve 1 corresponds to $\eta = 0.07$, curve 2 to $\eta = 0.14$, curve 3 to $\eta = 0.21$, curve 4 to $\eta = 0.37$, curve 5 to $\eta = 0.49$

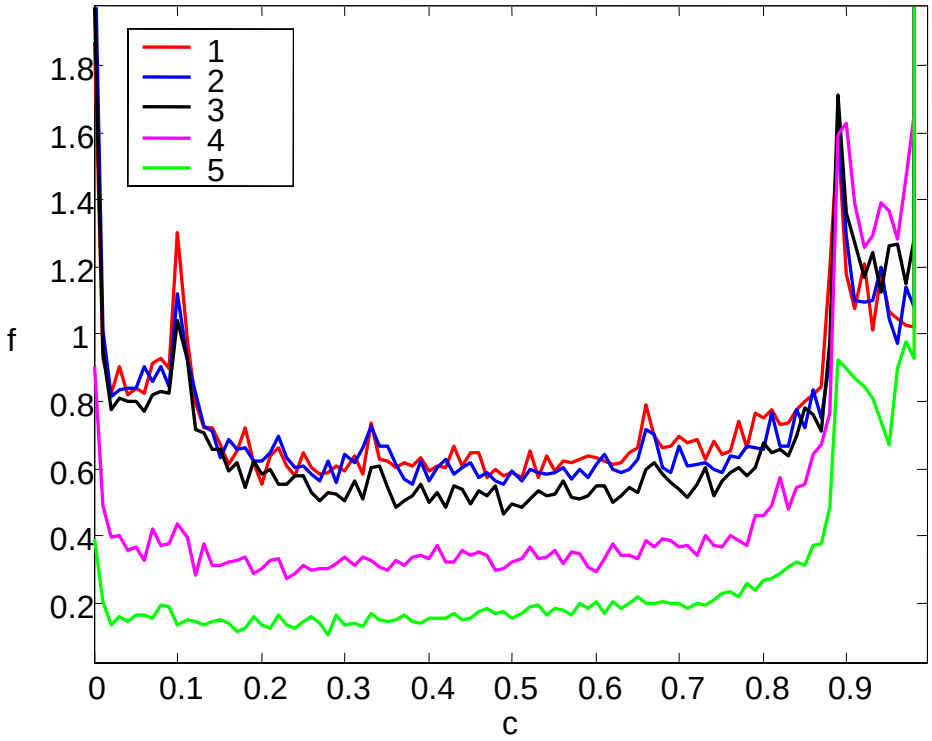

Fig. 16. Probability density function versus concentration, t=6.2 (M=100). Curve 1 corresponds to $\eta = 0.07$, curve 2 to $\eta = 0.14$, curve 3 to $\eta = 0.21$, curve 4 to $\eta = 0.37$, curve 5 to $\eta = 0.49$.